ORIGINAL ARTICLE

Conjugate heat transfer investigation of cooled turbine using the preconditioned density-based algorithm

Peng Wang[a], Yu Li[a,b], Zhengping Zou[a,*], Weihao Zhang[a]

[a]*National Key Laboratory of Science and Technology on Aero-Engine Aero-Thermodynamics, School of Energy and Power Engineering, Beihang University, Beijing 100191, China*
[b]*Beijing Institute of Nearspace Vehicle's Systems Engineering, Science and Technology on Space Physics Laboratory, Beijing 100076, China*

Abstract The preconditioned density-based conjugate heat transfer (CHT) algorithm was used to investigate the heat transfer characteristics of a cooled turbine vane. Fluid domain provided boundary heat flux for solid domain and obtained boundary temperature from it for the coupling strategy. The governing equations were solved by the preconditioned density-based finite-volume method, with preconditioning matrix, improved Abu-Gharmam Shaw (AGS) transition model, matrix dissipation scheme and four kinds of turbulence models. The grid system is multi-block structured grids for fluid domain and unstructured grids for solid domain, with full-matched grids at the fluid–solid interfaces. The effects of turbulence model, outlet Mach number, outlet Reynolds number, inlet turbulence intensity and the temperature ratio of blade surface/gas on the local heat transfer performance were studied. Results indicate that the k–ω shear-stress transport (SST) and AGS model can predict the conjugate heat transfer better than others. The Mach number and Reynolds number have relatively obvious influences on the heat transfer, while the turbulence intensity and temperature ratio only have slight influences. Comparisons with experimental data demonstrate the applicability and accuracy of the numerical algorithm.

*Corresponding author: Tel.: +86 10 82339125.

E-mail address: zouzhengping@buaa.edu.cn (Zhengping Zou).

Production and hosting by Elsevier

Nomenclature

C_p	specific heat at constant pressure
$\vec{F}_c$	x component of convective flux vector
$\vec{F}_v$	x component of diffusive flux vector
$\vec{G}_c$	θ component of convective flux vector
$\vec{G}_v$	θ component of diffusive flux vector
$\vec{H}_c$	r component of convective flux vector
$\vec{H}_v$	r component of diffusive flux vector
h	half height of duct
L	length of configuration
Ma	Mach number
M	transformation matrix form $\vec{W}$ to $\vec{W}_p$
M^{-1}	transformation matrix form $\vec{W}_p$ to $\vec{W}$
Pr	Prandtl number
P	pressure
$\vec{Q}$	source term
r	radius
R	gas constant
Re	Reynolds number
T	temperature
T_b	bulk temperature
T_{in}	inlet temperature
t	time
v_x	x component of velocity
v_θ	θ component of velocity
v_r	r component of velocity
$\vec{W}$	vector of conservative variables
$\vec{W}_p$	vector of primitive variables
x	x coordinate
$\overline{\Gamma}$	preconditioning matrix
γ	specific heat ratio
Δt	time step
θ	dimensionless temperature
ϕ	dimensionless temperature
μ	dynamic viscosity
τ	viscous shear stress
λ	thermal conductivity
Ω	control volume

Subscripts

f	fluid domain
in	inlet
s	solid domain
w	wall

1. Introduction

With the development of modern jet engines, the turbine inlet temperature would be further increased in order to enhance the thermal efficiency. The high temperature of hot gas far exceeds the permissible material temperature of turbine blades. Consequently, some methods must be taken to ensure the turbine blades against the high thermal loads. Currently, using a high efficiency cooling system is the common and primary way to cool blades and reduce their thermal loads. The precondition of designing a high efficiency cooling system is that the accurate temperature field of turbine blades is predicted. In the traditional method for predicting temperature field, the thermal boundary conditions must be specified and it requires tedious and costly iterations which involve sequentially numerical predictions of flow/temperature field of the hot gas and temperature field of blades. This method is a "decoupled" method and thus the results are unreliable. Instead, conjugate heat transfer (CHT) method is a more efficient and accurate way to predict temperature field. The flow/temperature field of the fluid (hot gas) and temperature field of solid (blades) are solved simultaneously. The temperature and heat flux are exchanged at fluid/solid interface at iterations. The CHT method is a "coupled" method and thus the results are more reliable.

The reliability of CHT method is proven by some researchers. Rigby and Lepicovsky [1] modified the Glenn-HT code to perform CHT simulations. Their approach extended the original solver to solid domain by imposing a constant density and a zero velocity in solid domain. At interfaces between solid and fluid, the code set the same wall temperature to produce a consistent heat flux. Heidmann [2] developed a finite volum method/boundry element method (FVM/BEM) coupled solver and numerically simulated the coupled flow/temperature fields of a realistic film-cooled turbine vane. The solver used for the fluid convection part of the problem was the Glenn-HT code. The solid conduction module was based on the BEM, and was coupled directly to the flow solver. Bohn et al. [3,4] developed a CHT code named CHT-flow, coupling a Navier–Stokes solver to a thermal code solving Fourier equation in the solid. He applied this solver to several CHT simulations for cooled turbine blades. Montomoli et al. [5] integrated a thermal solver for solid domain into an existing unstructured CFD solver HybFlow. The code was validated through two different test cases: a laminar flow over a flat plate and a film-cooled plate.

In the current paper, the CHT study for the complex Mark II turbine blade with radial cooling passages was conducted. In reference [6], the preconditioned density-based CHT algorithm was developed and adopted to solve the CHT problems such as the laminar/turbulent flow over a flat plate and the Sajben diffuser flow. The coupling of fluid and solid domains was accomplished through a common interface temperature T_w which ensured the balance of heat flux at interface. The governing equations were solved by the preconditioned density-based finite-volume method, with preconditioning matrix, matrix

dissipation scheme and four kinds of turbulence models. The numerical results indicated that the proposed numerical method had good numerical accuracy and applicability. For the CHT simulation in more complex situation such as cooling turbine, some expand and improvement are conducted for the algorithm in this paper. For example, the Abu-Gharmam Shaw (AGS) transition model is improved, the grid for solid domain can be unstructured and the coupling strategy is also expanded. On the basis of these, the effects of turbulence model, outlet Mach number, outlet Reynolds number, inlet turbulence intensity and the temperature ratio of blade surface/gas on the local heat transfer performance are analyzed. The numerical results are also compared with experimental data for demonstrating the applicability of the CHT method in cooling turbine.

2. Governing equations

2.1. Navier–Stokes equations

The Faver-averaged compressible Navier–Stokes (N-S) equations in frame of cylindrical coordinates $(x, r\theta, r)$ are solved in fluid domain [7]. These equations expressed in integral form over an arbitrary control volume Ω are

$$\frac{\partial}{\partial t}\int_{\Omega}\vec{W}\mathrm{d}\Omega + \oint_{\partial\Omega}\left\{\vec{F}_c n_x + \left(\vec{G}_c - \vec{W}\cdot v_{mg}\right)n_\theta + \vec{H}_c n_r\right\}\mathrm{d}S$$

$$= \oint_{\partial\Omega}\left(\vec{F}_v n_x + \vec{G}_v n_\theta + \vec{H}_v n_r\right)\mathrm{d}S + \int_{\Omega}\vec{Q}\mathrm{d}\Omega \tag{1}$$

where $\vec{W}$ is the vector of conservative variables and v_{mg} is the rotating speed. $(\vec{F}_c, \vec{G}_c, \vec{H}_c)$, $(\vec{F}_v, \vec{G}_v, \vec{H}_v)$ are the vectors of convective fluxes and viscous fluxes respectively, and $\vec{Q}$ is the vector of source terms. These vectors can be expressed as

$$\vec{W} = \begin{bmatrix} \rho \\ \rho v_x \\ \rho v_\theta r \\ \rho v_r \\ \rho E \end{bmatrix} \quad \vec{F}_c = \begin{bmatrix} \rho v_x \\ \rho v_x v_x + p \\ \rho v_x v_\theta r \\ \rho v_x v_r \\ \rho H v_x \end{bmatrix} \quad \vec{G}_c = \begin{bmatrix} \rho v_\theta \\ \rho v_x v_\theta \\ (\rho v_\theta v_\theta + p)r \\ \rho v_\theta v_r \\ \rho H v_\theta \end{bmatrix}$$

$$\vec{H}_c = \begin{bmatrix} \rho v_r \\ \rho v_x v_r \\ \rho v_r v_\theta r \\ \rho v_r v_r + p \\ \rho H v_r \end{bmatrix} \quad \vec{F}_v = \begin{bmatrix} 0 \\ \tau_{xx} \\ r\tau_{\theta x} \\ \tau_{rx} \\ \Theta_x \end{bmatrix} \quad \vec{G}_v = \begin{bmatrix} 0 \\ \tau_{x\theta} \\ r\tau_{\theta\theta} \\ \tau_{r\theta} \\ \Theta_\theta \end{bmatrix}$$

$$\vec{H}_v = \begin{bmatrix} 0 \\ \tau_{xr} \\ r\tau_{\theta r} \\ \tau_{rr} \\ \Theta_r \end{bmatrix} \quad \vec{Q} = \begin{bmatrix} 0 \\ 0 \\ 0 \\ (\rho v_\theta^2 + p - \tau_{\theta\theta})/r \\ 0 \end{bmatrix} \tag{2}$$

$$\Theta_x = v_r\tau_{xr} + v_\theta\tau_{x\theta} + v_x\tau_{xx} + \kappa\frac{\partial T}{\partial x}$$

$$\Theta_\theta = v_r\tau_{\theta r} + v_\theta\tau_{\theta\theta} + v_x\tau_{\theta x} + \kappa\frac{\partial T}{r\partial\theta}$$

$$\Theta_r = v_r\tau_{rr} + v_\theta\tau_{r\theta} + v_x\tau_{rx} + \kappa\frac{\partial T}{\partial r} \tag{3}$$

2.2. Turbulence models

The closure of the N–S equations is provided by the eddy-viscosity turbulence models. Four turbulence models are added to the code, including algebraic Bladwin–Lomax (BL) model [8], one-equation Spalart–Allmaras (SA) model [9], two-equation low-Reynolds Chien k–ε model [10] and k–ω shear-stress transport (SST) model [11].

To solve the "anomalous turbulent kinetic energy" problem in the leading-edge region of turbine blade, the P_k limiter of turbulent kinetic energy production term and the C_μ limiter based on "realizability" condition are employed to modify the Chien k–ε turbulence model.

2.3. Preconditioning method

In the low Mach number flow, the condition number becomes large. It would increase the stiffness of governing equations. Thus, the convergence of solution to steady state is slowed down. Furthermore, the accuracy of some spatial discretization schemes containing artificial dissipation terms suffer at low Mach numbers [12]. In order to solve the low Mach number flows efficiently and accurately, preconditioning method can be employed.

On the other hand, preconditioning method is also necessary in CHT simulations of cooling turbines. In order to cool turbine blades, the cooling systems inside the turbine are very complex. This may lead to low Mach number flows in cooling passages inside the turbine blades, but the flows outside the blades maybe subsonic or transonic, even supersonic. For this "all speed" type flow, the CHT simulations involving flows in the outer blade passages, heat conduction inside the blade and flows in the cooling passages would be suffered from difficulties without employing preconditioning. Thus, in order to efficiently and accurately predict the flow/temperature field outside/inside the blade and temperature field of blades, the preconditioning method is necessary and must be employed.

In the present paper, a preconditioning method based on Weiss and Smith preconditioning matrix [13] is implemented which could significantly accelerate the convergence and improve the accuracy of results. The integral form of preconditioning N–S equations for the conservative variables can be expressed as

$$\overline{\boldsymbol{\Gamma}} \cdot \boldsymbol{M}^{-1} \cdot \frac{\partial}{\partial t} \int_{\Omega} \vec{W} \mathrm{d}\Omega + \oint_{\partial\Omega} \left\{ \vec{F}_c n_x + \left(\vec{G}_c - \vec{W} \cdot v_{mg} \right) n_\theta + \vec{H}_c n_r \right\} \mathrm{d}S$$

$$= \oint_{\partial\Omega} \left(\vec{F}_v n_x + \vec{G}_v n_\theta + \vec{H}_v n_r \right) \mathrm{d}S + \int_{\Omega} \vec{Q} \mathrm{d}\Omega \qquad (4)$$

where $\boldsymbol{M}^{-1} = \frac{\partial \vec{W}_p}{\partial \vec{W}}$ and $\overline{\boldsymbol{\Gamma}}$ is the preconditioning matrix, and the detailed description can be found in Appendix A. $\vec{W}$ is the vector of the conservative variables and $\vec{W}_p$ is the vector of the primitive variables. The $\partial \vec{W}_p / \partial \vec{W}$ denotes the transformation matrix from $\vec{W}_p = (\rho, v_x, v_\theta, v_r, P)^{\mathrm{T}}$ to $\vec{W} = (\rho, \rho v_x, r\rho v_\theta, \rho v_r, \rho E)^{\mathrm{T}}$. It is given in Appendix A. Note that the Jacobians of convective flux are changed after preconditioning. Consequently, the artificial dissipation term of central scheme is also changed, which will be discussed in Section 3.

2.4. Fourier heat conduction equation

The capability of CHT calculation is accomplished by integrating a new heat conduction procedure into the flow solver. The heat conduction procedure solves the heat transfer Fourier equation in solid domain. The integral form of Fourier heat conduction equation is

$$\frac{\partial}{\partial t} \int_{\Omega} (\rho c T) \mathrm{d}\Omega = \oint_{\partial\Omega} \left[\left(\kappa \frac{\partial T}{\partial x} \right) n_x + \left(\kappa \frac{\partial T}{r \partial \theta} \right) n_\theta \right.$$

$$\left. + \left(\kappa \frac{\partial T}{\partial r} \right) n_r \right] \mathrm{d}S \qquad (5)$$

where Ω denotes the control volume, and S denotes the face of the control volume. T, ρ, c and κ denote the temperature, density, specific heat coefficient and thermal conductivity of the solid respectively.

2.5. Transition model

It is found by the author that the AGS transition model is not appropriate when heat fluxes through the wall are large. Therefore, an improved method, employing incompressible formulas instead of compressible formulas to compute boundary layer parameter, is proposed by the author. It is proved to be reasonable and effective by some CHT cases.

3. Numerical method

3.1. Spatial discretization for N–S equations

The governing equations are solved with a cell-vertex finite volume approach, as shown in Figure 1. Convective fluxes, diffusive fluxes and source terms are computed using the control volume Ω. Then the sums of them computed for the control volume Ω have to be distributed to cell vertexes using a non-weighted distribution formula [14]. The contribution of the artificial dissipation to the total residual is calculated using the control volume Ω' and then is added to the total residual directly.

3.1.1. Convective fluxes

Convective fluxes are computed using central differencing. The artificial dissipation is needed to prevent odd-even decoupling. Jameson scalar artificial dissipation [15] and matrix artificial dissipation [16] are added to the code to reduce the numerical dissipation. The discretization is formally second order accurate.

3.1.1.1. Scalar dissipation scheme. The artificial dissipation of Martinelli and Jameson [15] consists of a hybrid adaptive scheme of second and fourth order differences of the conservative variables along the coordinate directions i, j, k and is calculated for the control volume Ω' as follows (for example, $(i + 1/2, j, k)$ face)

$$\vec{D}_{i+\frac{1}{2},j,k} = \lambda_{i+\frac{1}{2},j,k} \left[\varepsilon^{(2)}_{i+\frac{1}{2},j,k} \left(\vec{W}_{i+1,j,k} - \vec{W}_{i,j,k} \right) \right.$$
$$\left. - \varepsilon^{(4)}_{i+\frac{1}{2},j,k} \left(\vec{W}_{i+2,j,k} - 3\vec{W}_{i+1,j,k} + 3\vec{W}_{i,j,k} - \vec{W}_{i-1,j,k} \right) \right]$$

$$(6)$$

The definitions of λ, $\varepsilon^{(2)}$ and $\varepsilon^{(4)}$ are provided in [8].

3.1.1.2. Matrix dissipation scheme. In order to improve the accuracy by reducing the numerical dissipation, the preceding Scalar scheme can be modified to become more like an upwind scheme. The idea is to use a matrix (the convective flux Jacobian) instead of the scalar value λ to scale the dissipation terms [16]. In this way, each equation is scaled properly by the corresponding eigenvalue. Hence,
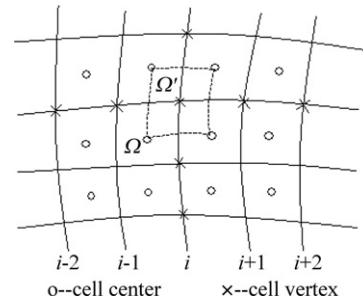

i-2 i-1 i i+1 i+2
o--cell center   ×--cell vertex

Figure 1 Control volume sketch.

the Eq. (6) becomes

$$\vec{D}_{i+\frac{1}{2},j,k} = |A_c|_{i+\frac{1}{2},j,k} \left[\varepsilon^{(2)}_{i+\frac{1}{2},j,k} \left(\vec{W}_{i+1,j,k} - \vec{W}_{i,j,k} \right) \right.$$
$$\left. - \varepsilon^{(4)}_{i+\frac{1}{2},j,k} \left(\vec{W}_{i+2,j,k} - 3\vec{W}_{i+1,j,k} + 3\vec{W}_{i,j,k} - \vec{W}_{i-1,j,k} \right) \right] \Delta S_{i+\frac{1}{2},j,k}$$

$$(7)$$

The scaling matrix corresponds to the convective flux Jacobian $(A_c = \partial \vec{F}_c / \partial \vec{W})$ diagonalised with absolute values of the eigenvalues

$$|A_c| = T |A_c| T^{-1} \tag{8}$$

with T as the right eigenvector, T^{-1} as the left eigenvector and Λ_c as the diagonal matrix of the eigenvalues.

3.1.1.3. Modified scalar/matrix dissipation scheme with preconditioning.

Since the convective flux Jacobian is changed after preconditioning, the artificial dissipation term of central scheme would be also changed. According to [17], the above Eq. (6) and Eq. (7) become

$$\vec{D}_{i+\frac{1}{2},j,k} = P_{i+\frac{1}{2},j,k} \left| \sigma(P^{-1}A_c) \right|_{i+\frac{1}{2},j,k} \vec{d}_{i+\frac{1}{2},j,k}$$
$$\vec{d}_{i+\frac{1}{2},j,k} = \left[\varepsilon^{(2)}_{i+\frac{1}{2},j,k} \left(\vec{W}_{i+1,j,k} - \vec{W}_{i,j,k} \right) \right.$$
$$\left. - \varepsilon^{(4)}_{i+\frac{1}{2},j,k} \left(\vec{W}_{i+2,j,k} - 3\vec{W}_{i+1,j,k} + 3\vec{W}_{i,j,k} - \vec{W}_{i-1,j,k} \right) \right]$$

$$(9)$$

where $P = \overline{T}M^{-1}$ and $\sigma(\bullet)$ is a function. If $\sigma(A) \sim \lambda(A)$, we would have a scalar dissipation. If $\sigma(A) \sim A$, we would have a matrix dissipation. For scalar dissipation scheme, the expression is

$$\vec{D}_{i+\frac{1}{2},j,k} = P_{i+\frac{1}{2},j,k} \overline{\lambda}_{i+\frac{1}{2},j,k} \vec{d}_{i+\frac{1}{2},j,k}$$
$$\left(\overline{\lambda} \text{ is spectral radius of } P^{-1}A_c \right) \tag{10}$$

For matrix dissipation scheme, the expression is

$$\vec{D}_{i+\frac{1}{2},j,k} = P_{i+\frac{1}{2},j,k} \left| P^{-1}A_c \right|_{i+\frac{1}{2},j,k} \vec{d}_{i+\frac{1}{2},j,k} \tag{11}$$

where $\left| P^{-1}A_c \right| = \overline{T} |\overline{\Lambda}| \overline{T}^{-1}$. An efficient way to compute the product of Jacobians $\left| P^{-1}A_c \right|$ with different vector $\vec{d}$ is provided in [18].

3.1.2. Diffusive fluxes

Diffusive fluxes are computed using central differencing with a "viscous body force" method. The gradients of flow variables are first calculated at the cell centers by integrating over the control volume Ω. In the next step, the "viscous body force" is calculated at cell centers by the sum of force at cell faces. Finally, the sum of diffusive fluxes at cell vertexes are computed by distributing the "viscous body force" from cell centers to cell vertexes.

3.2. Temporal discretization for N–S equations

The spatial discretization of preconditioning N–S equations is written as

$$\overline{T}M^{-1}\Omega \frac{\Delta \vec{W}}{\Delta t} = -\sum \left(\vec{F}^{(c)} - \vec{F}^{(v)} \right) \Delta S + \Omega \cdot \vec{Q} = -\vec{R} \tag{12}$$

$$\Delta \vec{W} = -\frac{\Delta t}{\Omega} \left(M\overline{T}^{-1}\vec{R} \right) \tag{13}$$

The Eq. (13) is integrated in time using an explicit single-stage "SCREE" scheme which is given by

$$\Delta \vec{W}^n = \left\{ 2 \left(\frac{\Delta \vec{W}}{\Delta t} \right)^n - \left(\frac{\Delta \vec{W}}{\Delta t} \right)^{n-1} \right\} \Delta t \tag{14}$$

The solver utilizes local time-stepping, implicit residual smoothing [19] and multi-grid to accelerate convergence to steady state.
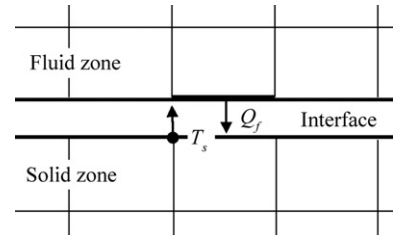

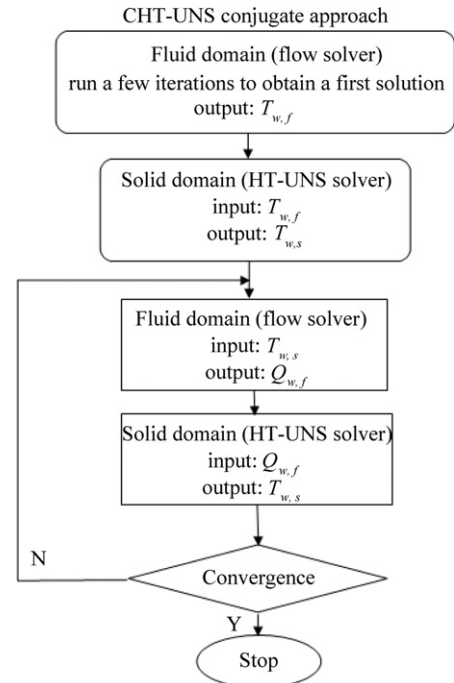**Figure 2** Transfer of temperature and heat flux at interfaces.

Figure 3 Scheme of conjugate algorithm.

3.3. Spatial and temporal discretization for turbulence model equations

The turbulence model equations are solved using a similar cell-vertex scheme with N–S equations. The only difference is that the source terms of turbulence model equations are computed using the control volume Ω'. Convective and diffusive fluxes are also computed using central differencing.

A coupled algorithm is used to solve the N–S equations and the turbulence model equations with the same time-stepping scheme. Local time-stepping, residual smoothing and multi-grid are applied uniformly to both the N–S equations and the turbulence model equations.

3.4. Spatial and temporal discretization for Fourier equation

The spatial and temporal discretization schemes of heat conduction procedure are identical with that of flow solver. Diffusive fluxes are computed using central differencing and the time-stepping scheme is also the "SCREE" scheme.

3.5. Computational grid and conjugate strategy

The grid system is multi-block structured grids for fluid domain and unstructured grids for solid domain with full-matched or non-matched grids at the fluid-fluid interfaces and full-matched grids at the fluid–solid interfaces. The coupling of fluid domain and solid domain is accomplished through the transfer of temperature and heat flux at interfaces, as shown in Figure 2.

The main steps required to implement for a CHT calculation are shown in Figure 3. In order to reduce computational cost and iteration number, a first flow solution is achieved after an imposed iteration number, without any computation in solid domain. The computed temperature distributions of solid boundaries are transfer to the heat conducting solver and then it starts to solve the Fourier equation in solid domain. After that, fluid domain obtains boundary temperature from solid domain and solid domain obtains boundary heat flux from fluid domain. This algorithm proceeds iteratively until the convergence is achieved.

4. Geometric modeling and computational grid

The Mark II configuration has been designed and tested by Hylton et al. [20,21] to provide a data base for testing the predictive capabilities of analytical models [22,23]. Their investigations cover a wide range of operating conditions and geometries.

Figure 4 shows the geometric configuration and the computational grid. The blade is cooled by ten cooling
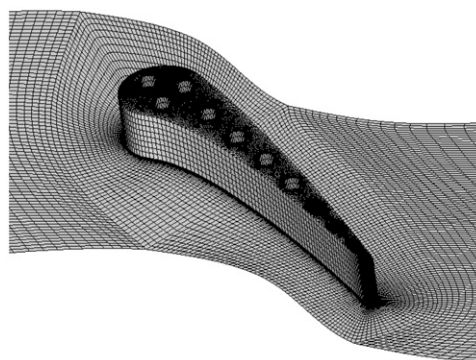

Figure 4   Computational grid.

Table 1   Mainstream boundary condition of 4411.

Boundary condition	Value
Inlet	
Total temperature/K	784
Total pressure/Pa	342,255
Turbulence intensity	0.065
Mach number	0.18
Reynolds number	5.8×10^5
Outlet	
Static pressure/Pa	204,560
Mach number	0.89
Reynolds number	1.98×10^6

channels, supplied with air. Trailing edge of the blade has a blunt shape. The grid has a resolution of 151,623 structured grid points in the fluid domain and 105,696 unstructured grid points in the solid domain. Computational domain is a quarter of the blade height and 9 layers of grids are set in the radial direction. The two end surfaces in radial direction of fluid domain and solid domain are set as periodic boundaries. The fluid in cooling channels is not simulated and the heat transfer coefficient of the channel surface is determined by the method in reference [20]. This method has also been used in reference [24–26] and the results of the method are credible.

The tests of different conditions are identified by a series of number in original references. If there is no special note, the simulations of Mark II turbine in this paper are all corresponding to the condition of 4411. The mainstream boundary condition of 4411 is showed in Table 1.

5. Results and discussion

It is well known that there are many factors have influences on the heat transfer at blade surface. They are the transition characteristics of boundary layer, free stream turbulence intensity, Mach number, Reynolds number, pressure gradient, the reaction of shock wave and boundary layer and so on. In combination with the

experimental data of Hylton et al., the influence of turbulence model on heat transfer is firstly study and then the authors study the effects of Mach number, Reynolds number, turbulence intensity and the temperature ratio of blade surface and mainstream gas.

5.1. Influence of turbulence model

The influences of different turbulence models (with transition) on flow and heat transfer inside turbine are investigated. The turbulence models are BL and AGS model, SA and AGS model, Chien k–ε and AGS model and k–ω SST and AGS model.

Figure 5 shows the temperature fields at blade middle section corresponding to different turbulence models. It can be found from the fields that the gas temperature near leading edge stagnation point is relatively high. A shock wave appears at suction side and the gas speed suddenly drops, temperature quickly increases. The flow at pressure side is relatively smooth and the temperature does not have obvious change towards stream wise. Because of the cooling effect of the cooling channels, the temperature of blade domain is lower than mainstream locally.

As the figures show, the flow fields in the flow passage are obviously different due to the different prediction ability of turbulence models in flow. The difference in flow would influence the heat transfer performance at blade surface and then the temperature field in the blade domain would be also different.

Figure 6 shows the temperature distributions at blade surface of different turbulence models, and the experimental data is also given. The positive value of X/L represents the suction side of blade and the negative value represents the pressure side. As the figure shows, the predicted temperature distributions at blade surface by different turbulence models are obviously different.
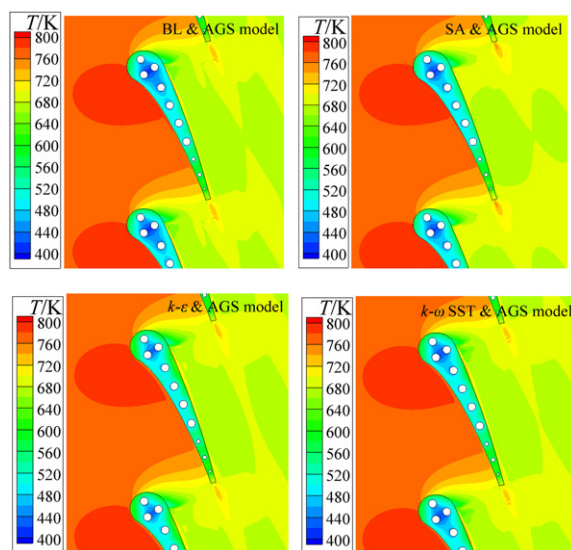
Figure 5   Temperature fields at blade middle section of different turbulence models (with transition model).
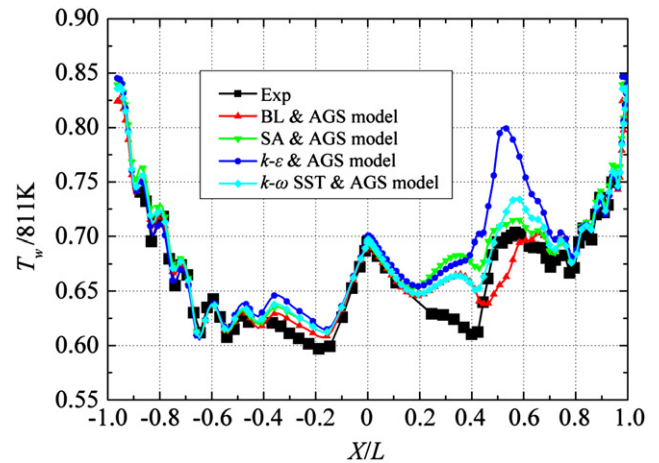
Figure 6   Temperature distributions at blade surface of different turbulence models (with transition model).

At the pressure surface, the temperature distributions predicted by four turbulence models are almost the same at most area except the area of $X/L \approx [-0.4, -0.2]$ where a little difference can be seen. All of the results at pressure surface can match well with the experimental data and the maximum difference between numerical and experimental data is less than 2.5% (relative to the reference temperature 811 K).

At the leading edge beginning area ($X/L \approx [0, 0.2]$) of suction surface, the temperature distributions of four models have little difference and match well with experimental data. Following this area, the boundary layer begins to have transition in the area of $X/L \approx [0.2, 0.43]$ before the shock wave and all of the results of four models are obviously different with experimental data. The reason is that the transition prediction performance of AGS model is still not perfect enough, especially in the flow with shock wave, and it makes that the predicted beginning and end points of transition are not accurate enough. In this area, the results of k–ω SST and AGS model and BL and AGS model relatively match well with the experimental data.

In the area after the shock wave ($X/L \approx [0.43, 0.7]$), interaction of shock wave and boundary layer exist. The prediction performances of models for this kind of flow are different, so the results are obviously different with each other. The results are also different with the experimental data. In this area, the Chien k–ε and AGS model has the maximum difference with the experimental data, while the k–ω SST and AGS model and the SA and AGS model have relatively little difference with the experimental data.

Comprehensively, the k–ω SST and AGS model can make the best prediction which is matching well with the experimental data. Following are the SA and AGS model and the BL and AGS model. The Chien k–ε and AGS model has the worst prediction performance in the four models. For the results of k–ω SST and AGS model, the maximum difference with experimental data at suction

surface is less than 5% and less than 2% at the pressure surface.

Figure 7 shows the heat transfer coefficient distributions at blade surface predicted by different turbulence models and also the experimental data. The heat transfer coefficient at blade surface is defined as the following relation

$$H = \frac{Q_{w,f}}{T_{gas} - T_{w,f}} \frac{\kappa_{w,f} (\partial T / \partial n)_{w,f}}{T_{gas} - T_{w,f}} \quad (15)$$

where T_{gas} is the total temperature at mainstream inlet, $Q_{w,f}$ is the heat flux of fluid domain surface. H_0 is the reference value of heat transfer coefficient. For the 4411 condition, $H_0 = 1135 \ (W \cdot m^2 \cdot K)$.

As the figure shows, as same as the temperature distribution in Figure 6, the heat transfer coefficient distributions at pressure side all match well with the experimental data while the results near shock wave ($X/L \approx [0.2, 0.7]$) at suction surface are obviously different with experimental data. Comprehensively, the k–ω SST and AGS model, SA and AGS model and BL and AGS model have the similar accuracy in predicting the heat transfer coefficient and the k–ε and AGS model has a worse performance. For the results of k–ω SST and AGS model, the maximum difference with experimental data at pressure surface is less than 5% (relative to the reference value) and less than 5% at most area of the suction surface except the area near the shock wave.

For further proving the heat transfer prediction performance of the turbulence model conducted in this paper, Figure 8 shows the comparison of the k–ω SST and AGS model in this paper and the k–ω SST and γ–θ model in the commercial software CFX. The results of k–ω SST and γ–θ model are catched from reference [27] and its computational model and condition are the same as this paper.

As can be seen in Figure 8(a) of temperature distributions, the results of k–ω SST and AGS model are better than k–ω SST and γ–θ model at most area except
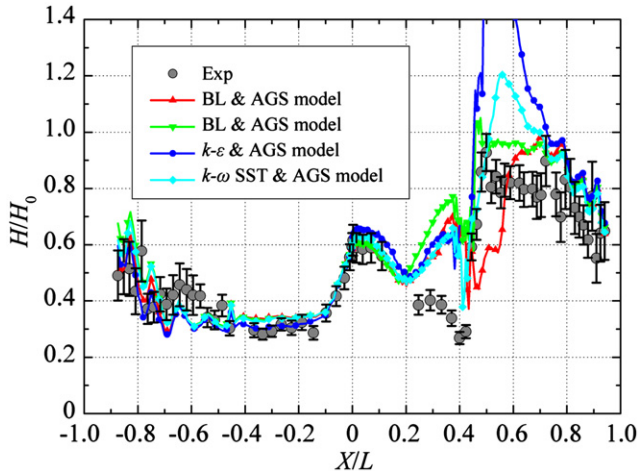

Figure 7 Heat transfer coefficient distributions at blade surface predicted by different turbulence models (with transition model).
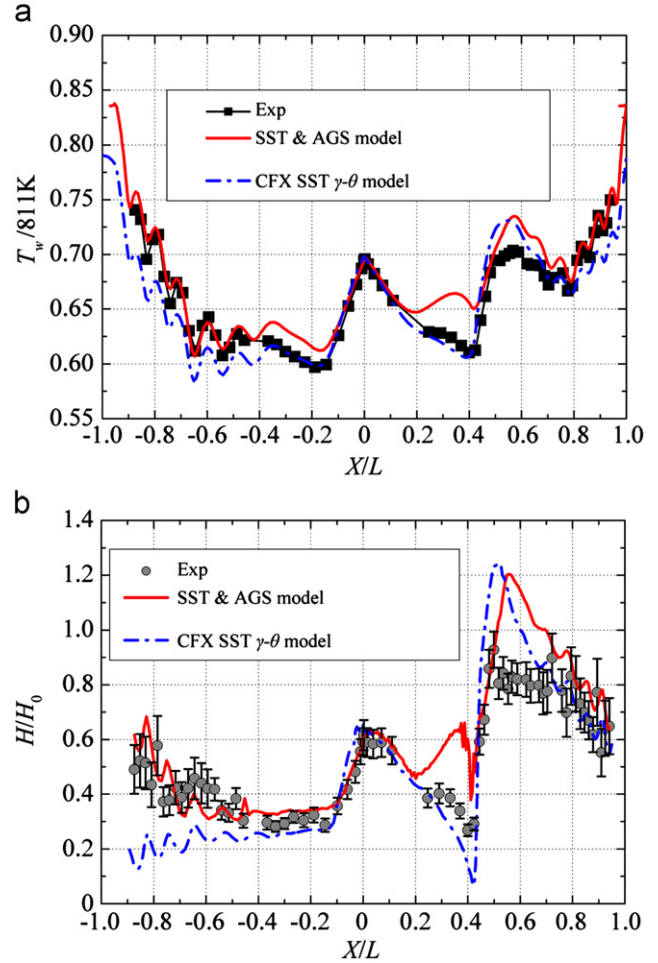

Figure 8 Comparison of blade surface temperature and heat transfer coefficient distributions(k–ω SST and AGS and k–ω SST and γ–θ).

the transition area at suction surface ($X/L \approx [0.2, 0.43]$) and the area of $X/L \approx [-0.4, -0.2]$ at pressure surface. Especially in the second half of the pressure surface, the results of k–ω SST and γ–θ model are relatively lower while the results of k–ω SST and AGS model match well with the experimental data. The heat transfer coefficient distributions in Figure 8(b) have similar characteristics with the temperature distribution in Figure 8(a). Comprehensively, the prediction of transition location at suction side by k–ω SST and AGS model is not better than k–ω SST and γ–θ model but the prediction of transition at pressure side is better than it. Generally speaking, the results of the k–ω SST and AGS model in this paper rival those of k–ω SST and γ–θ model or even better than it. The k–ω SST and AGS model is selected for the rest of studies in this paper.

5.2. Influence of outlet Mach number

Secondly, the influence on blade surface heat transfer of the blade outlet isentropic Mach number (Ma_2) is studied. The conditions numbered 4411 and 5411 in the

experiments are selected. Most of the conditions of them are similar except Ma_2. The Ma_2 of 4411 is subsonic with the value of 0.89 and 5411 is supersonic with 1.04.

Figure 9 shows the Mach number fields at blade middle section in the conditions of different Ma_2. As the figures show, the flow in blade passage is obviously affected by Ma_2. At the suction side, there is only one shock wave in the 4411 condition of subsonic outlet while there are two shock waves in the 5411 condition of supersonic outlet.

Figure 10 shows the blade surface pressure and temperature distributions in the two conditions and the experimental data is also given for comparison. As the figures show, the numerical results of the method in this paper match well with the experimental data. It can be seen from Figure 10(a) that the increase of Ma_2 almost has no influence on the pressure distribution at pressure side while the influence on suction side can be seen after the location of $X/L \approx 0.43$ (the location of shock wave/separation). Figure 10(b) shows that the increase of Ma_2 would make the blade surface temperature decrease slightly and this characteristic is similar with the experimental result.

For investigating the influence of Ma_2 on blade surface heat transfer characteristics, Figure 11 shows the comparison of blade surface heat transfer coefficient in the two conditions and the experimental results are also given.

Similar with the pressure distributions in Figure 10(a), the change of Ma_2 almost has no influence on heat transfer at the pressure side and the area before separation ($X/L < 0.43$) in suction surface. But in the area after the separation point, the influence can be seen. When the Ma_2 increases, the heat transfer coefficient after separation point at suction surface begins to decrease. It can be seen from the comparison of numerical and experimental results that the method in this paper can prediction well the change tendency of heat transfer coefficient after separation point at suction side and the change amplitudes also match well with the experimental data.

It can be seen from the change of heat transfer coefficient at pressure side and suction side that there is an obvious relationship between the heat transfer coefficient distribution and the pressure distribution
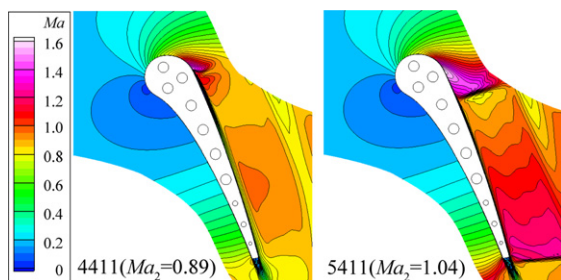

Figure 9 Mach number fields at blade middle section in the conditions of different Ma_2 (4411 and 5411).
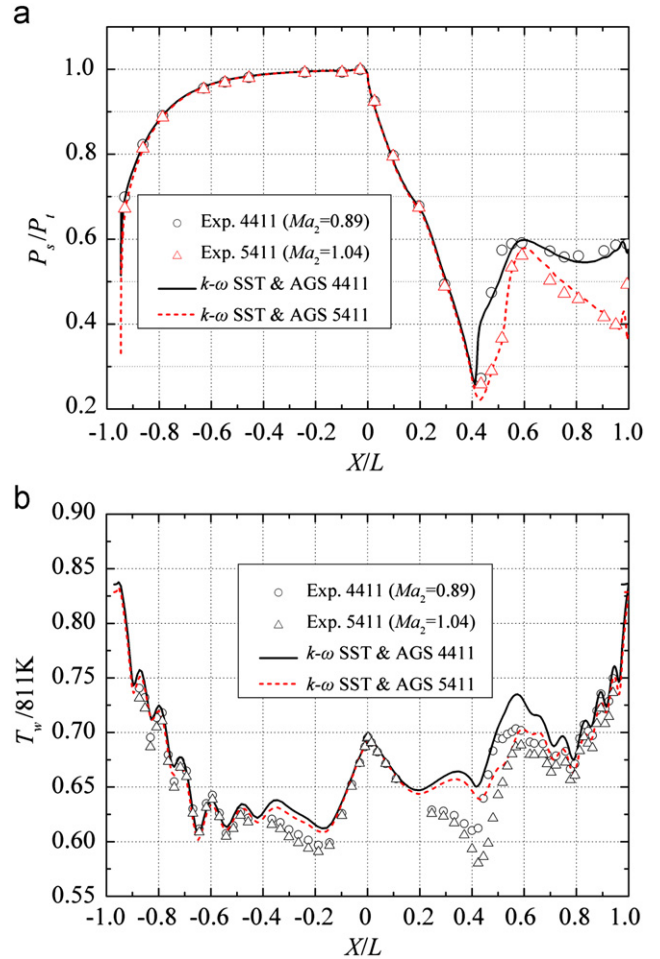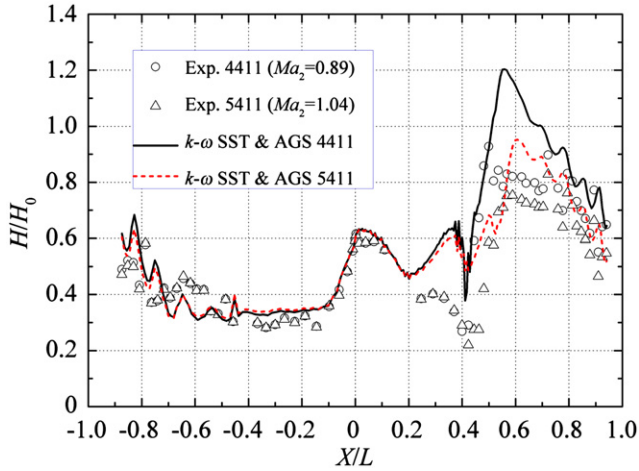

Figure 10 Pressure and temperature distributions in conditions of different Ma_2 (4411 and 5411).

when the outlet Mach number changes. The distribution of heat transfer coefficient does not change in the area where the pressure distribution does not change and obviously change in the area pressure change.

5.3. Influence of outlet Reynolds number

Subsequently, the influence of blade passage outlet Reynolds number (Re_2) on blade surface heat transfer is studied. The conditions numbered 4311, 4411 and 4511 in the experiments are selected. Most of the conditions of them are similar except Re_2. The Re_2 of 4311 is 1.56×10^6, 4411 is 1.98×10^6 and 4511 is 2.46×10^6.

Figure 12 shows the pressure and temperature distributions at blade surface in conditions of different Re_2. As the Figure 12(a) shows, the pressure distributions of three conditions are nearly the same because of the similar inlet and outlet Mach number. It can be seen from Figure 12(b) that the temperature at blade surface increases following the increase of outlet Reynolds number. The temperature distributions of 4311 and 4411 conditions have only a little difference while the temperature of 4511 condition is obviously higher. The
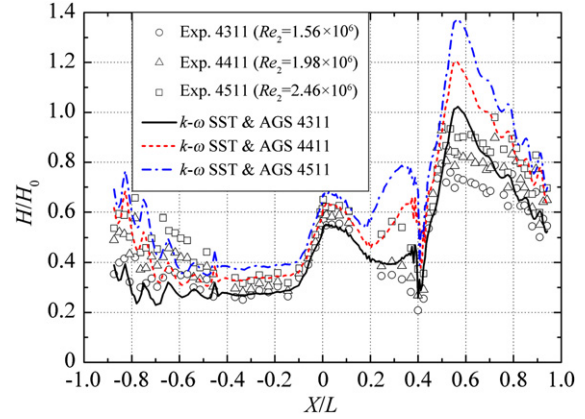
Figure 11 Blade surface heat transfer coefficient distributions in conditions of different Ma_2 (4411 and 5411).
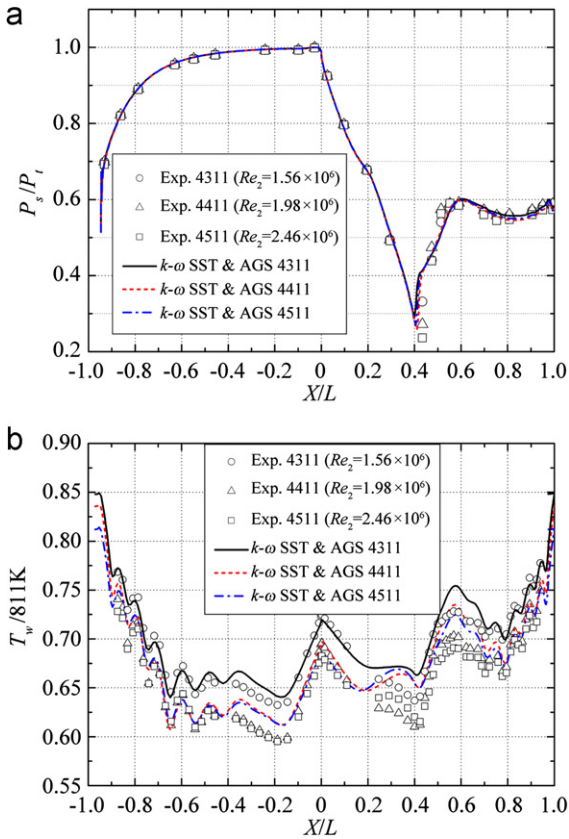
Figure 12 Pressure and temperature distributions at blade surface in conditions of different Re_2 (4311, 4411 and 4511).

results of this paper predict well the temperature change tendency and amplitude with the change of Re_2.

Figure 13 shows the comparison of blade surface heat transfer coefficient in the three conditions and the experimental results are also given. It can be seen from the figure that the result of this paper capture well the increase tendency of heat transfer coefficient


Figure 13 Heat transfer coefficient distributions at blade surface in conditions of different Re_2 (4311, 4411 and 4511).

corresponding to the increase of Reynolds number. For the Mark II blade experiment in reference [20], Hylton points out that the influence of Re_2 on the blade surface heat transfer coefficient mainly reflects in the integral translation of the coefficient and the detailed distribution law has no large change. The numerical results in this paper also show this phenomenon.

The experimental data shows that all of the heat transfer coefficient distributions at suction surface in three conditions have a suddenly increase (at the location of transition). The locations are all near to $X/L \approx 0.43$ where the shock wave/separation happens. This means that the transition location at suction surface is almost not influenced by Reynolds number and the change of heat transfer coefficient is mainly controlled by the flow separation. The transition location at suction side predicted in this paper is not exact enough, but it still can be seen that the transition location is almost not effected by Reynolds number and the suddenly increase of heat transfer coefficient at separation point is also predicted well.

At the pressure surface, the experimental data of heat transfer coefficient shows that the heat transfer coefficient at the back of blade have a more obvious increase tendency when the Reynolds number increase. It indicates that the transition location at pressure side changes and the change of heat transfer coefficient is mainly influenced by the transition (the transition at pressure is a typical bypass transition). The numerical results at pressure side also well indicate this phenomenon. For $Re_2 = 1.56 \times 10^6$ in 4311 condition, heat transfer coefficient increases obviously after $X/L \approx 0.8$. For higher Reynolds number in 4411 condition and 4511 condition, heat transfer coefficients increase obviously after $X/L \approx 0.6$.

For indicating the influence of Reynolds number on the flow transition at pressure side, Figure 14 shows the intermittency factor distributions at pressure surface. It can be seen that the transition location at pressure side moves to upstream leading edge following the increase of Reynolds number.
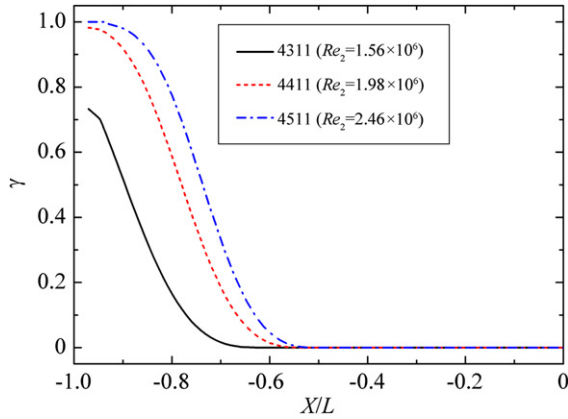
Figure 14 Intermittency factor distributions at pressure surface in conditions of different Re_2 (4311, 4411 and 4511).
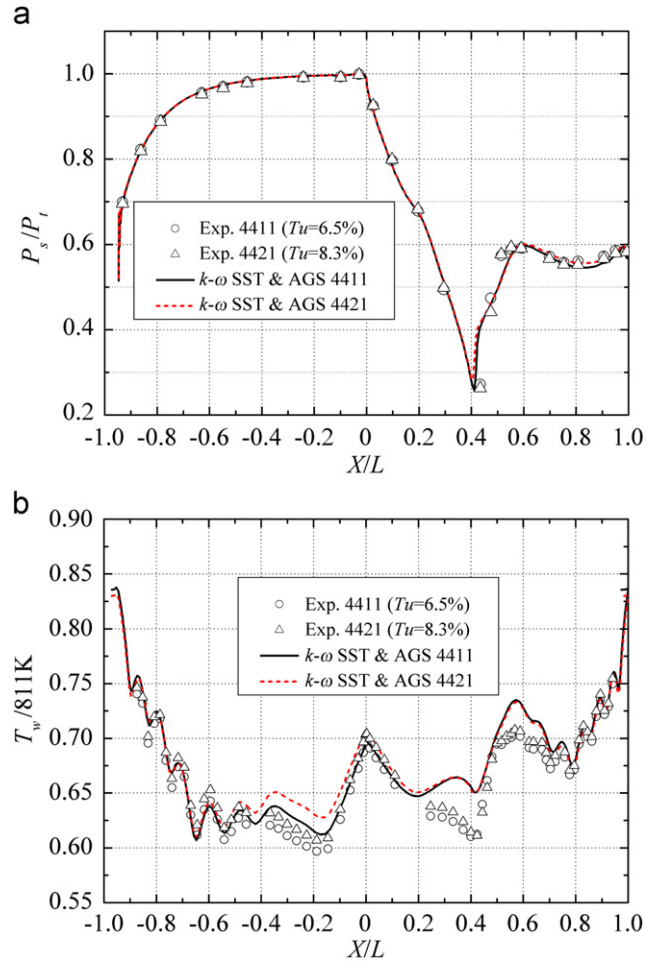
5.4. Influence of inlet turbulence intensity

The influence of blade passage inlet turbulence intensity (Tu) on blade surface heat transfer is studied. The conditions numbered 4411 and 4421 in the experiments are selected. Most of the conditions of them are similar except Tu. The Tu of 4411 is 6.5% and 4421 is 8.3%.

Figure 15 shows the pressure and temperature distributions at blade surface in conditions of different inlet turbulence intensity and the corresponding experimental data is also given.

It can be seen from Figure 15(a) that the pressure distributions is almost not affected by the change of inlet turbulence intensity. As Figure 15(b) shows, temperature at blade surface increases when the inlet turbulence intensity increases. The influence of Tu on the temperature distributions is relatively large in the front of blade where the flow is laminar and has not start transition; the influence is relatively small in the turbulent area after transition.

Figure 16 shows the comparison of heat transfer coefficient distributions at blade surface. As the figure shows, the heat transfer coefficient at blade surface has a slight increase when the Tu increases. Both of the experimental and numerical results show that the transition location at blade surface basically has no change. The experimental data indicates that the change of heat transfer coefficient on the blade surface mainly reflects in the integral translation of the coefficient with increase and the detailed distribution law has no large change. In the numerical results, the change tendency of heat transfer coefficient caused by Tu can be well predicted in the laminar area before transition and the change amplitude is also similar with the experimental data. However, the difference of heat transfer coefficient distributions of the two conditions is relatively small in the turbulent area after transition. The reason is that the turbulence attenuation speed predicted by the turbulence model is relatively quick and then the slight

Figure 15 Pressure and temperature distributions at blade surface in conditions of different Tu (4411 and 4421).

difference of turbulence intensity in the two conditions at the back of blade cannot be captured.

5.5. Influence of temperature ratio of blade surface/gas

Finally, the influence of temperature ratio of blade surface/gas (Tw/Tg) on blade surface heat transfer is studies. The conditions numbered 4411 and 4412 in the experiments are selected. Most of the conditions of them in mainstream are similar except Tw/Tg. The Tw/Tg of 4411 is 0.69 and 4412 is 0.79.
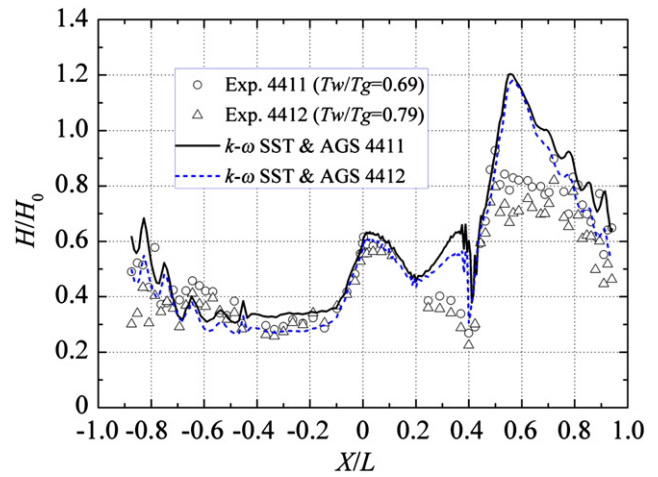
Figure 17 shows the pressure and temperature distributions at blade surface in conditions of different Tw/Tg. As Figure 17(a) shows, the change of Tw/Tg has no obvious influence on the pressure distribution. Figure 17(b) shows that the temperature at blade surface obviously increases when the Tw/Tg increases. It is because of the detailed boundary conditions.

Figure 18 shows the heat transfer coefficient distributions at blade surface in conditions of different Tw/Tg. As the
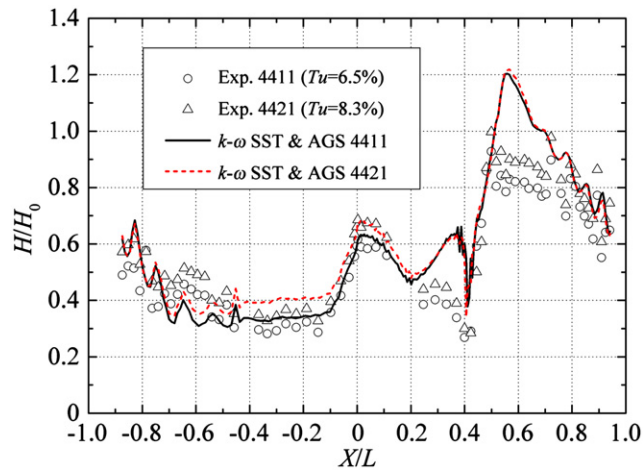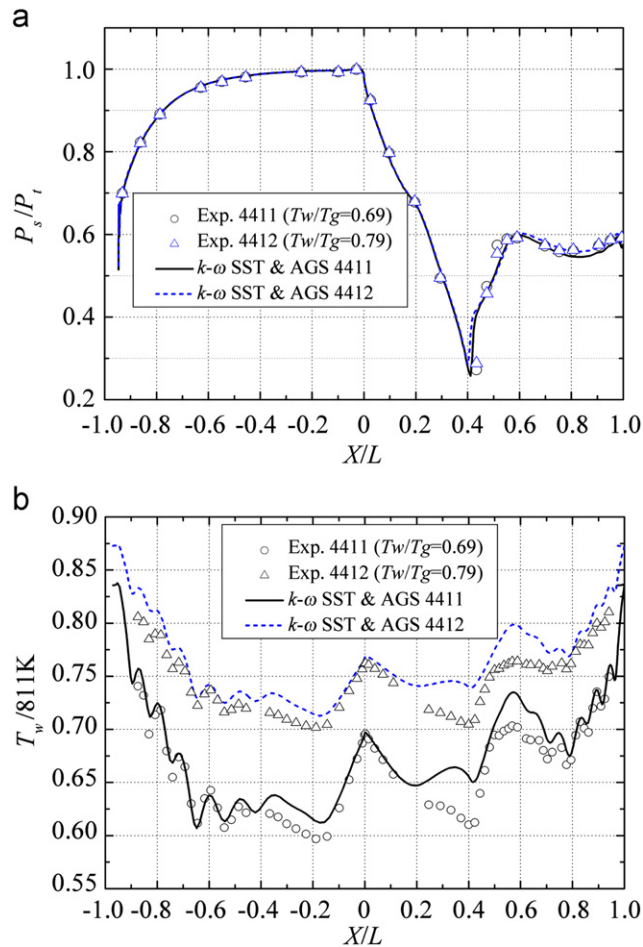
Figure 16 Heat transfer coefficient distributions at blade surface in conditions of different Tu (4411 and 4421).

Figure 18 Heat transfer coefficient distributions at blade surface in conditions of different Tw/Tg (4411 and 4412).

Figure 17 Pressure and temperature distributions at blade surface in conditions of different Tw/Tg (4411 and 4412).

figure shows, the influence of the Tw/Tg change on the heat transfer coefficient distribution is not obvious and the coefficient has a decrease tendency when the Tw/Tg increases. The figure also shows that the heat transfer coefficient distributions are nearly the same in different conditions in the leading edge laminar area before

transition. However, the influence of different conditions is relatively obvious in the turbulence area after transition ($X/L > 0.6$ in the suction side for example).

6. Conclusion

The preconditioned density-based conjugate heat transfer (CHT) algorithm is used to investigate the heat transfer characteristics of a cooled turbine vane. Fluid domain provides boundary heat flux for solid domain and obtains boundary temperature from it for the coupling strategy. The governing equations are solved by the preconditioned density-based finite-volume method, with preconditioning matrix, improved AGS transition model, matrix dissipation scheme and four kinds of turbulence models. The grid system is multi-block structured grids for fluid domain and unstructured grids for solid domain, with full-matched grids at the fluid–solid interfaces.

The effects of turbulence model (with transition model), outlet Mach number, outlet Reynolds number, inlet turbulence intensity and the temperature ratio of blade surface/gas on the local heat transfer performance are studied. The comparisons with experimental data demonstrate the applicability and accuracy of the numerical algorithm. The following conclusions can be drawn.

1. For the conjugate heat transfer of turbine blade, the prediction performances of different turbulence models have relatively obvious difference. The difference mainly can be seen at the suction side while the predicted results at pressure side are similar. Compared with experimental data, the prediction accuracy with these models at suction side is lower than pressure side because of the complex flow at suction side. Comprehensively, the heat transfer prediction performance of k–ω SST and AGS model is the best in the four and following are the BL and AGS and SA and AGS model. The performance of k–ε and AGS model is

relatively bad because of the stubborn defect with too large turbulent kinetic energy prediction in the boundary layer after shock wave. For the SST and AGS model in this paper, its prediction accuracy is not lower than the SST and γ-Re_θ model in commercial software CFX.

2. The change of outlet Mach number almost has no influence on the pressure side heat transfer. For the suction side, the influence can be seen after the separation point and the heat transfer coefficient in this area decreases when the Mach number increases. These characteristics have obvious relation with the pressure distribution at blade surface.

3. The heat transfer coefficient at blade surface obviously increases when the Reynolds number increases. This change tendency is mainly integral translation and the detailed distribution has no large change. The transition location at suction side is basically not effected by the change of Reynolds number and the transition location at pressure side moves to upstream leading edge when Reynolds number increases.

4. The heat transfer coefficient has a slight increase when the inlet turbulence intensity increases (6.5%–8.3%). The transition location almost has no change because of the change amplitude of inlet turbulence intensity is relatively slight.

5. The heat transfer coefficient has a slight decrease when the blade surface/gas temperature ratio (Tw/Tg) increases (0.7–0.8). In the laminar area before transition, Tw/Tg has a very slight influence on the heat transfer coefficient. In the turbulence area after transition, Tw/Tg has a relatively large influence on the heat transfer coefficient.

Acknowledgments

Appendix A

A1. Preconditioning matrix

In frame of cylindrical coordinates($x,r\theta,r$), the preconditioning matrix $\overline{T}$ defined in Eq. (4) is given by

$$\overline{T} = \begin{bmatrix} \theta & 0 & 0 & 0 & \rho_T \\ \theta v_x & \rho & 0 & 0 & \rho_T v_x \\ r\theta v_\theta & 0 & r\rho & 0 & r\rho_T v_\theta \\ \theta v_r & 0 & 0 & \rho & \rho_T v_r \\ \theta H-\delta & \rho v_x & \rho v_\theta & \rho v_r & \rho_T H + \rho C_p \end{bmatrix} \qquad (16)$$

where $\rho_T = \frac{\partial \rho}{\partial T}\big|_{p\,=\,\text{const}}$. For the ideal gas, $\rho_T = -p/RT^2 = -\rho/T$. The parameter θ is given by

$$\theta = \frac{1}{u_r^2} - \frac{\rho_T}{\rho C_p} \qquad (17)$$

and $\delta = 1$ ($\delta = 0$ for compressible fluid). The reference velocity u_r is defined as

$$u_r = \min\left[c, \max\left(|\vec{v}|, \quad \frac{\upsilon}{\Delta x}, \quad \varepsilon\sqrt{\frac{\Delta p}{\rho}}\right)\right] \qquad (18)$$

The definitions of terms in Eq. (18) can be found in [13].

A2. Transformation matrix

The transformation matrix $\frac{\partial \vec{W}_p}{\partial \vec{W}}$ defined in Eq. (4) are given by

$$\frac{\partial \vec{W}_p}{\partial \vec{W}} = \begin{bmatrix} \hat{q}^2 & (1-\gamma)v_x & \frac{1}{r}(1-\gamma)v_\theta & (1-\gamma)v_r & \gamma-1 \\ -\dfrac{v_x}{\rho} & \dfrac{1}{\rho} & 0 & 0 & 0 \\ -\dfrac{v_\theta}{\rho} & 0 & \dfrac{1}{r}\dfrac{1}{\rho} & 0 & 0 \\ -\dfrac{v_r}{\rho} & 0 & 0 & \dfrac{1}{\rho} & 0 \\ \dfrac{\hat{q}^2-RT}{\rho R} & \dfrac{(1-\gamma)v_x}{\rho R} & \dfrac{1}{r}\dfrac{(1-\gamma)v_\theta}{\rho R} & \dfrac{(1-\gamma)v_r}{\rho R} & \dfrac{\gamma-1}{\rho R} \end{bmatrix} \qquad (19)$$

where $q^2 = v_x^2 + v_\theta^2 + v_r^2$ and $\hat{q}^2 = \frac{(\gamma-1)q^2}{2}$. R is specific gas constant and γ is ratio of specific heat coefficients.

References

[1] D.L. Rigby, J. Lepicovsky, Conjugate heat transfer analysis of internally cooled configurations, ASME Paper 2001-GT-0405, 2001.

[2] J.D. Heidmann, A.J. Kassab, E.A. Divo, F. Rodriguez, E. Steinthorsson, Conjugate heat transfer effects on a realistic film-cooled turbine vane, ASME Paper GT2003-G38553, 2003.

[3] D. Bohn, B. Bonhoff, H. Schonenborn, H. Wilhelmi, Validation of a numerical model for the coupled simulation fluid flow and diabatic walls with application to film-cooled gas turbine blades, VDI-Berichte, Nr. 1186, 1995.

[4] D. Bohn, B. Bonhoff, H. Schonenborn, Combined aerodynamic and thermal analysis of a turbine nozzle guide vane, in: Proceedings of the 1995 Yokohama International Gas Turbine Congress, IGTC-paper-108, 1995.

[5] F. Montomoli, F. Adami, S.D. Gatta, F. Martelli, Conjugate heat transfer modelling in film cooled blades, ASME Paper GT2004-53177, 2004.

[6] Y. Li, Z.P. Zou, A 3-D preconditioning conjugate heat transfer solver and validation, in: Proceedings of the 3rd International Symposium Jet Propulsion and Power Engineering, Nanjing, China, September 13–17, 2010, Paper No. 2010-ISJPPE-2001.

[7] J.D. Denton, The calculation of three-dimensional viscous flows through multistage turbomachines, ASME Journal of Turbomachinery 114 (1) (1992) 18–26.

[8] B.S. Baldwin, H. Lomax, Thin layer approximation and algebraic model for separated turbulent flows, in: Proceedings of the 16th Aerospace Sciences Meeting, edited by AIAA, Huntsville, USA, 16–18 January, 1978, pp. 78–257.

[9] P.R. Spalart, S.R. Allmaras, A one-equation turbulence model for aerodynamic flows, AIAA Paper 92-0439, 1992.

[10] K.Y. Chien, Predictions of channel and boundary-layer flows with a low-Reynolds-number turbulence model, AIAA Journal 20 (1) (1982) 33–38.

[11] F.R. Menter, Two-equation eddy-viscosity turbulence models for engineering applications, AIAA Journal 32 (8) (1994) 1598–1605.

[12] D. Lee, Local preconditioning of Euler and Navier–Stokes equations, Ph.D. Thesis, University of Michigan, Ann Arbor, MI, 1996.

[13] J. Weiss, W.A. Smith, Preconditioning applied to variable and constant density flows, AIAA Journal 33 (11) (1995) 2050–2057.

[14] M.G. Hall, Cell-vertex multigrid scheme for solution of the Euler equations in: K.W. Morton, M.J. Baines (Eds.), Proceedings of the International Conference on Numerical Methods for Fluid Dynamics, Oxford, UK, 1986.

[15] L. Martinelli, A. Jameson, Validation of a multigrid method for the Reynolds averaged equations, AIAA-88-0414, 1988.

[16] R.C. Swanson, E. Turkel, Aspects of a high resolution scheme for the Navier–Stokes equations, in: Proceedings of the 11th Computational Fluid Dynamics Conference, edited by AIAA, Orlando, USA, July 6–9, 1993, Paper No. 93-3372.

[17] E. Turkel, V.N. Vatsa, R. Radespiel, Preconditioning methods for low-speed flows, AIAA Paper 96-2460, 1996.

[18] J.E. Anker, J.F. Mayer, A preconditioned solution scheme for the simulation of turbomachinery flow at arbitrary Mach numbers, AIAA Paper 2004-762, 2004.

[19] E. Turkel, R.C. Swanson, V.N. Vatsa, J.A. White, Multigrid for hypersonic viscous two- and three-dimensional flows, AIAA Paper 91-1572, 1991.

[20] L.D. Hylton, M.S. Mihelc, M. Turner, D.A. Nealy, R. York, Analytical and experimental evaluation of the heat transfer distribution over the surfaces of turbine vanes, NASA Technical Report CR 168015, 1983.

[21] D.A. Nealy, M.S. Mihelc, L.D. Hylton, H.J. Gladden, Measurements of heat transfer distribution over the surfaces of highly loaded turbine nozzle guide vanes, ASME Paper 83-GT-53, 1983.

[22] E.J. Hall, D.A. Topp, R.A. Delaney, Aerodynamic/heat transfer analysis of discrete site film-cooled turbine airfoils, AIAA 94-3070, 1994.

[23] K.H. Kao, M.S. Liou, On the application of chimera/unstructured hybird grids for conjugate heat transfer, ASME Paper 96-GT-156, 1996.

[24] L. Lin, J. Ren, H.D. Jiang, Application of $\gamma - Re_\theta$ transition model for internal cooling simulation, Journal of Engineering Thermophysics 30 (11) (2009) 1849–1852 (in Chinese).

[25] Z.F. Wang, P.G. Yan, H.F. Tang, H.Y. Huang, W.J. Han, Study on inner-cooling channels heat transfer coefficient criteria formula of a high pressure air-cooled turbine, Journal of Engineering Thermophysics 31 (2) (2010) 247–250 (in Chinese).

[26] C. Zhou, Q. Wang, Z.Y. Guo, J.H. Huang, G.T. Feng, Coupled heat transfer analysis of air cooling gas turbine, Journal of Propulsion Technology 30 (5) (2009) 566–570 (in Chinese).

[27] B. Liu, Numerical simulation of low Reynolds number effects on turbine flow and heat transfer performance, Dissertation for the Degree of Master, Beihang University, Beijing, 2010 (in Chinese).